Generation of virtual lithium-ion battery electrode microstructures based on spatial stochastic modeling

Daniel Westhoff[a,*], Ingo Manke[b], Volker Schmidt[a]

[a] *Ulm University, Institute of Stochastics, Helmholtzstr. 18, 89069 Ulm, Germany*
[b] *Helmholtz-Zentrum Berlin, Institute of Applied Materials, Hahn-Meitner-Platz 1, 14109 Berlin, Germany*

Abstract

It is well known that the microstructure of the active material in lithium-ion battery electrodes has a strong influence on the battery's performance. In order to improve functional properties of lithium-ion batteries, designing optimized electrode morphologies is an important task. As exploring a large set of possible design concepts via laboratory experiments is very expensive in cost and time, model-based simulations have become an important tool to explore a broad range of possible microstructures on the computer. They allow a preselection of promising design concepts. This procedure, which is called virtual materials design, involves two main tasks. First, a tool for creating virtual, but realistic electrode morphologies is needed. This tool must be able to generate a broad range of electrode microstructures on the computer. In a second step, the performance of these virtual electrodes must be evaluated using spatially resolved numerical transport simulations. In the present paper, the first part of this procedure is addressed. A general framework based on tools of stochastic geometry is presented, which can be used to create a broad range of different electrode microstructures on the computer. To demonstrate the wide spectrum of possible outcomes of the microstructure generator as well as its ability to describe real electrode microstructures, we show how the microstructure of three types of electrodes, which exhibit rather different morphologies, can be described using different adaptions of the framework. A comparison of structural characteristics of the model outputs and tomographic image data of real electrodes indicates a good fit of the model. Moreover, we show how design concepts can be implemented for generating virtual electrode microstructures that can be used as input for spatially resolved transport simulations.

Keywords: Lithium-ion battery, virtual materials design, electrode microstructure, stochastic microstructure modeling, energy cell, power cell

*Corresponding author
Email address: daniel.westhoff@uni-ulm.de (Daniel Westhoff)

1. Introduction

Although lithium-ion batteries are, due to their high energy density, widespread in many applications [1], production costs are high while the energy density is still too small for an entirely satisfying application in the automotive sector [2]. As it is well-known that the microstructure of battery electrodes strongly influences their performance [3], it is highly desired to identify optimal electrode morphologies. With laboratory experiments being expensive in cost and time, many approaches are based on modeling and simulations, see, e.g., [4]. In [5], a tool for spatially resolved electrochemical transport simulations has been developed, which has recently, e.g., been applied to analyze properties of thick electrodes [6]. However, for systematic investigations of the relationships between the microstructure of electrodes and their electrochemical properties, it is necessary to have a broad range of electrode microstructures as input for spatially resolved electrochemical simulations. In the present paper, a framework for such a microstructure generator is described. The basic idea is to model the individual active particles of the electrodes using spherical harmonics expansions of Gaussian random fields. Note that spherical harmonics can be used to represent functions defined on a sphere, see [7] for an overview. Modeling of particles using spherical harmonics has successfully been performed in [8] and [9]. In [10], an approach to ensure a realistic arrangement and connectivity of particles in the sampling window is presented for modeling of battery electrodes. This method is extended in [11, 12]. The modeling approaches considered in [10, 11, 12] are based on tools of stochastic geometry [13]. The main idea is to subdivide the region of interest into a space-filling system of polytopes, a so-called Laguerre tessellation, see [14] for details on this topic. Subsequently, the individual particles are placed inside the polytopes, where a pre-defined connectivity of particles is ensured using a connectivity graph (see [15] for details on graphs). While exhibiting a remarkably good fit to experimental data for different scenarios (anodes in energy and power cells as well as pristine and aged cathodes), these models also have some limitations which make their application for virtual materials testing difficult. On the one hand, the model construction via Laguerre tessellations is rather complicated and the number of parameters is quite large, and, on the other hand, the parameters are rather abstract variables with no direct geometrical interpretation. This makes it difficult to systematically vary and adjust morphological parameters. For instance, even predetermining a specific particle size distribution is difficult, as the particle size distribution can not be directly expressed as a function of model parameters. Therefore, in the present paper a simplified version of these models is presented, where the number of model parameters is kept small, and many model parameters have a direct geometrical interpretation. In particular, the particle size distribution is a direct, adjustable input parameter. The basic idea is to omit the construction via a random tessellation, and, instead, use a random packing of spheres to control the spatial arrangement of particles. These spheres are subsequently replaced with particles which are generated using spherical harmonics, whereby their volume is retained. This procedure has

three main advantages. First, as already mentioned above, the particle size distribution can be directly adjusted by predetermining the size distribution of the spheres being packed. Moreover, sphere packing algorithms are reproducing the production process of electrodes in a more natural way than the approach via tessellations, i.e., a random packing of spheres can be interpreted to mimic the random allocation of particles when casting the suspension of an electrode. It turns out that, surprisingly enough without further presets, this approach leads to a good representation of how particles are in contact with each other in real data. Finally, the small number of parameters, which mainly have a direct geometrical interpretation, allows for a systematic variation of morphological properties.

The model described in the present paper is constructed in a modular concept, which consists of three main modules. Each module can be adjusted to the specific needs in a given application, where "adjustment" does not only mean a different choice of parameters, but slightly changing the setup of the individual modules. We first present the general framework with a simple example, i.e., each of the modules is kept in the most simple way. Afterwards, we show how the three modules can be adjusted to three different battery scenarios, anodes in energy and power cells as well as cathodes. Finally, we give examples for adjusting the modules for generating virtual electrode microstructures. The modular concept has the great advantage that a collection of slightly different implementations of each module can be created. When generating virtual structures, a choice for each module can be made and the different modules can be combined with each other.

Note that the framework described in the present paper is not only applicable for lithium-ion battery electrodes, but similar methods can be used to model other particulate materials.

The outline of the paper is as follows. The general framework of the modeling idea is presented in Section 2. Examples using specific adaptions of the framework are presented in Section 3. For the three examples under consideration, a comparison of structural characteristics of model realizations and tomographic image data is performed to show that the simulation outcomes are realistic. Applications for virtual materials design using the framework are described in Section 4. Conclusions are drawn in Section 5.

Note that in Section 4 only two examples for the generation of virtual microstructures are presented. For an overview of further virtual structures that can be generated using the framework described in the present paper, we refer to the supplementary material.

2. Modeling framework

2.1. Overview

In order to model a system of connected particles, three main steps are necessary. This is (a) modeling of locations and approximate sizes of particles, (b) determining how particles should be in contact with each other and (c)

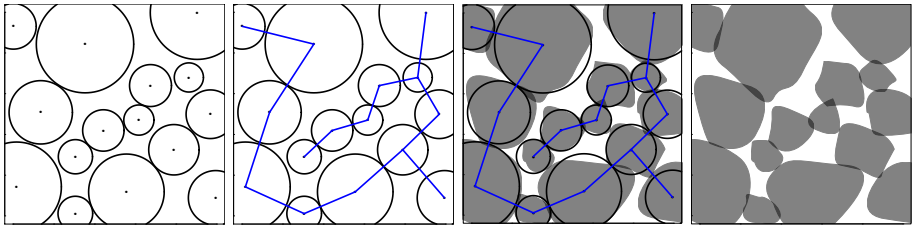

(a) (b) (c) (d)

Figure 1: (a) Approximate locations and sizes of particles are modeled using a random allocation of spheres (black circles). This can, e.g., be achieved using the force-biased algorithm for random sphere packing. (b) A connectivity graph (blue) determines how particles should be connected with each other. This can, e.g., be the minimum spanning tree. (c) For each sphere, a particle with approximately the same size is modeled using a Gaussian random field on the sphere (grey), where the connectivity conditions are fulfilled. (d) Spheres and graph are deleted and only the (connected) system of particles is retained.

modeling of particles themselves according to the specifications of the first two steps. These steps are illustrated as a 2D sketch in Figure 1. A 3D view can be found in Figure 2. The main difference of the approach proposed in the present paper compared to the ones in [10, 11, 12] is to use a random packing of spheres in the first step instead of random tessellations. These spheres act as a placeholder for the particles that will be created in a later step. Thus, they define their approximate locations and sizes. We will denote this set of random spheres by $\Xi = \{(S_i, R_i), i = 1, ..., N\}$ with $S_i \in W \subset \mathbb{R}^3$ a random vector in the sampling window W, a random radius $R_i > 0$ of the corresponding sphere and N the random number of spheres in the sampling window. Such a random packing of spheres with predefined radii can be generated using the force-biased algorithm [16, 17]. Based on these spheres, a connectivity graph $G = (V, E)$ is constructed, where the vertex set $V = \Xi$ is the system of spheres, and the edgeset $E \subset \Xi \times \Xi$ consists of pairs of spheres. If there is an edge between two spheres, this indicates that the corresponding particles are supposed to touch each other. In contrast to the tessellation-based approach, in a random allocation of spheres generated by a packing algorithm it is much easier to implement such connectivity conditions, due to the fact that, if two spheres (almost) touch each other, it is easy to model two touching particles with the same volume as the spheres. The particles themselves are finally modeled using Gaussian random fields on the unit sphere, where the connectivity conditions can be reached by sampling from conditional multivariate normal distributions, which is possible by solving systems of linear equations.

In the following subsections, each modeling step is described in more detail. An example of a simple implementation of each step is given, which results in the example structure discussed in Section 2.5. Further implementations of the individual steps tailored to specific situations are discussed in Section 3.

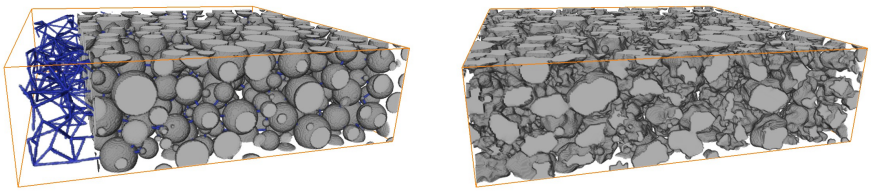

Figure 2: Left: Random sphere packing (grey) and connectivity graph (blue) in 3D. Right: System of particles simulated based on sphere packing and connectivity graph on the left.

2.2. Modeling of particle locations and sizes

In the first step, the approximate locations and sizes of particles are determined. These two features can be interpreted as a system of spheres, where the location of the sphere determines the approximate location of the particle, and the radius of the sphere determines its approximate size (as a volume-equivalent radius of the particle). A common tool to simulate such a random packing of spheres is the force-biased algorithm [16, 17, 18]. Based on an initial configuration of (overlapping) spheres, an iterative rearrangement is performed until the spheres do not overlap any more. The initial configuration is achieved as follows. Sphere radii are sampled from the desired particle size distribution $\mathcal{R}$, where throughout this paper, particle sizes will be considered as volume-equivalent radii. Spheres with radii drawn from $\mathcal{R}$ are thrown into the sampling window at random until the sum of volumes of all spheres divided by the volume of the sampling window exceeds a certain threshold ξ. The threshold ξ is chosen as the desired volume fraction of the active material in the electrode that is modeled. After iterative rearrangements, this results in a system of non-overlapping spheres $\Xi = \{(S_i, R_i), i = 1, ..., N\}$, where the sphere radii follow the desired particle size distribution $\mathcal{R}$ and the volume fraction of the sphere system in the sampling window matches the desired volume fraction of the active material in the battery electrode. For a visualization, see the 2D sketch in Figure 1(a) and the spheres in Figure 2, left. This is the basis for the next modeling step.

Note that not necessarily a random packing of spheres has to be used, but other approaches that lead to a system of marked points Ξ on W, e.g., random marked point processes, can also be used. However, for the examples discussed in the present paper, a random packing of spheres leads to reasonable results, which indicates that for a broad range of structures random packings of spheres can be used for the first modeling step.

Using the random sphere packing allows to directly control the approximate volume fraction ξ of the active material as well as the particle size distribution $\mathcal{R}$. Moreover, further characteristics can be controlled. For instance, in a slightly

modified version, the approximate pore size distribution can be regulated, see Section 3.3.

2.3. Modeling of particle connectivity

Given the approximate locations and sizes of particles, it has to be determined which particles should be in contact with each other. We use a geometric graph to describe connectivity of particles, see [15] for details on graphs. Often the aim is to achieve a completely connected system of particles, i.e., there is a path through the system of particles from each particle to every other particle. Thus, a good starting point for predetermining connectivity is the minimum spanning tree [19]. This is the subgraph of a completely connected graph with minimum sum of edge lengths in which a path from each vertex to every other vertex exists. Thereby, the (Euclidean) edge length can also be replaced by other weightings of edges. In our case, the set of vertices is the set of centers of the spheres Ξ. To prevent unrealistic particle configurations, we do not compute the minimum spanning tree from the graph with full connectivity, i.e., there is an edge between every pair of vertices, but from the graph G', where an edge is put between each sphere $(S_i, R_i) \in \Xi$ and its κ nearest neighbours and the distance is computed by the distance of sphere centers. Then, the minimum spanning tree G of G' is computed. Thereby the edges are weighted by the distance between centers of spheres minus both corresponding radii, which gives the shortest distance between the surfaces of both spheres. For an example of such a graph, see Figure 1(b) and the blue lines in Figure 2, left. Note that theoretically it is possible that G', and therewith G, is not completely connected, however, for reasonable large values of κ this does hardly happen.

In the next step (see Section 2.4), instead of spheres, not necessarily spherical particles will be created that touch each other as prescribed by G. In many cases, the minimum spanning tree is already sufficient, as it provides a completely connected system of particles. Contact of further particles will automatically happen due to the sphere packing approach, see Section 3.1. The reason for this is that, if two spheres are close to each other (because they have just been shifted to a non-overlapping position in the force-biased algorithm), volume-equivalent particles will touch each other with a high probability. If, however, further presets should be made by the connectivity graph, additional edges can be added to G. This allows a further predetermination of the structure of the particle system. An example is given in Section 3.2, where the connectivity graph is used to include anisotropy effects.

2.4. Modeling of particle shapes

In the final step, each sphere (which only acts as a placeholder) is replaced by a (not necessarily spherically shaped) particle. Thereby it is ensured that particles are in contact as predetermined by the connectivity graph and that the shape of simulated particles is drawn from the distribution of particle shapes observed in the given electrode that is being modeled. In order to do so, particles are modeled using Gaussian random fields on the unit sphere $\psi : [0, \pi] \times [0, 2\pi] \to$

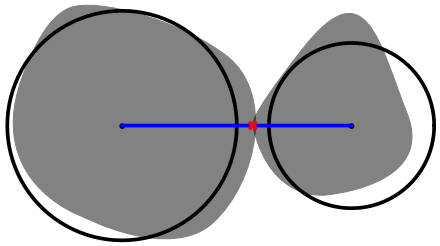

Figure 3: 2D sketch showing how particles are connected according to the connectivity graph. Black: Two spheres from the set Ξ. Blue: Edge of the connectivity graph. Red: Point which both particles have to touch. Grey: Particles sampled from the Gaussian random field model conditioned on the fact that they touch the red point. Thus, they are in contact with each other.

$\mathbb{R}$, where $\psi(\theta, \phi)$ describes the distance from the centroid of the particle to its boundary in direction (θ, ϕ). Isotropic Gaussian random fields are uniquely determined by their mean radius μ and the so-called angular power spectrum $A : [0, \infty) \to [0, \infty)$, see [20]. Furthermore, $\psi(\theta, \phi)$ can be represented using so-called spherical harmonic functions via

$$\psi(\theta, \phi) \approx \sum_{l=0}^{L} a_{l,0} Y_{l,0}(\theta, \phi) + 2 \sum_{m=1}^{l} \mathrm{Re}(a_{l,m}) \mathrm{Re}(Y_{l,m}(\theta, \phi)) - \mathrm{Im}(a_{l,m}) \mathrm{Im}(Y_{l,m}(\theta, \phi)).$$

In this formula, $Y_{l,m} : [0, \pi] \times [0, 2\pi) \to \mathbb{C}$ for $l \in \mathbb{N}_0$ and $m \in \{0, .., l\}$ denotes a spherical harmonic function for each l and m, $\mathrm{Re}(c)$ is the real part of a complex number $c \in \mathbb{C}$ and $\mathrm{Im}(c)$ its imaginary part, respectively. Moreover, the random coefficients $a_{l,m}$ are independent and normal distributed. In particular, $a_{0,0} \sim \mathcal{N}(\mu, A_0)$, $a_{l,0} \sim \mathcal{N}(0, A_l)$ for $l > 0$, $\mathrm{Re}(a_{l,m}) \sim \mathcal{N}(0, A_l/2)$ and $\mathrm{Im}(a_l, m) \sim \mathcal{N}(0, A_l/2)$ for $l \in \mathbb{N}$, $m \in \{1, ..., l\}$ with $A_l = A(l)$ and $\mathcal{N}(\cdot, \cdot)$ the normal distribution. For details on the spherical harmonic representation of particles, we refer to [9]. The parameter L is used to truncate the first sum, where for $L = \infty$ equality holds. In [9], it has been shown that rather small values of L can lead to a realistic description of particles extracted from tomographic image data, while at the same time a smoothing effect is achieved, i.e., artefacts from the imaging procedure or postprocessing are removed.

Using the concept described above, random particles can be generated by determining their mean radius μ and the angular power spectrum A. Then, a realization can be drawn by sampling from a multivariate normal distribution. The angular power spectrum can be estimated, e.g., from tomographic image data of a real particle system that is going to be modeled, see [10]. For each

particle, the mean radius μ is chosen to be the radius R_i of the sphere (S_i, R_i) that is replaced by the particle. Moreover, the connectivity conditions between two particles induced by the connectivity graph G can be met by forcing both particles to touch one or several joint points in space. This point can, e.g., be the (uniquely determined) point in space with shortest distance to both spheres, see the red cross in Figure 3. Then, a conditional multivariate normal distribution can be used to generate a particle that touches the given point(s), see [10] for details. By doing so for each sphere $(S_i, R_i) \in \Xi$, a particle system which is connected according to the connectivity graph G is generated, see also Figure 1(c) and Figure 2, right. Note that, due to the normal distribution of $\psi(\theta, \phi)$, it is possible that some values of $\psi(\theta, \phi)$ are negative, which is not desired (as we want the particle radius considered from its center to be always positive). We address this problem using an acceptance-rejection method, as it has also been done in [12]. Whenever a particle with negative radius in some direction occurs, this particle is rejected and a new particle is drawn from the considered multivariate normal distribution. This is done up to η times, where, unless otherwise stated, throughout this paper $\eta = 100$ is used. If after η runs still no particle with only positive radii in all directions is drawn, a sphere is generated the radius of which is drawn such that all connectivity conditions according to G are fulfilled. This however only happens for rather small particles, the size of which will only be a few voxels in the discretized image anyway. For larger particles, negative radii occur only with such a low probability that 100 repetitions typically lead to a realization with only positive radii.

2.5. Simple example

In this section, a simple implementation of the modeling framework is used to create a first example of a virtual microstructure. The microstructure is simulated in a sampling window with $500 \times 500 \times 200$ voxels, where voxels are cubic with a side length of 440nm. The sphere packing is generated as described in Section 2.2 with $\xi = 0.6$ and the particle size distribution $\mathcal{R}$ is chosen as a gamma distribution with shape parameter $k = 4$ and scale parameter $\theta = 4$ (remember that particle sizes are given as volume-equivalent radii). For the connectivity graph, the minimum spanning tree G with $\kappa = 10$ as described in Section 2.3 is chosen. For the angular power spectrum, the function

$$A(l) = \frac{al + b}{l^2 + cl + d}, \tag{1}$$

is considered, see also [10, 11, 12], where we put $a = 0.1027$, $b = 0.2411$, $c = -4.009$ and $d = 4.206$. These values have been obtained when modeling particles in NMC-cathodes in [12], and thus lead to rather regular particles with a high sphericity. In [12], the parameter L has been chosen individually for each particle. In this example, we globally set $L = 14$. The high sphericity and regularity of particles can be seen in Figure 4(a), where a realization of the model is shown. The volume fraction of the particle phase is 59.8% in this realization. In Figure 4(b), the particle size distribution of the model realization is compared

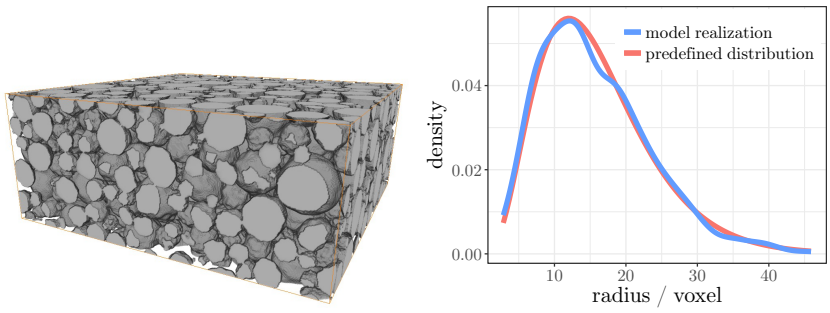

(a) (b)

Figure 4: (a) 3D example electrode microstructure generated by a simple implementation of the modeling framework. (b) Particle size distribution $\mathcal{R}$.

to the desired (gamma) particle size distribution. A nearly perfect match can be observed. Thus, this first example shows how the modeling framework can be implemented with only a few parameters to model an electrode microstructure with predefined volume fraction, particle size distribution and shape of particles. In Section 3, several further examples are given which show how the framework can be tailored to specific applications. Finally, in Section 4, its application for the generation of a wide spectrum of virtual, but realistic microstructures that can be used for virtual materials testing is shown.

2.6. Remarks on implementation

The modeling framework is implemented using the GeoStoch software library [21]. The advantages of the modular concept have already been addressed in Section 1. On the level of implementation, the modular concept can be visualized as shown in Figure 5. On the left-hand side, an interface for each of the three main steps of the algorithm is shown. Given all these models, the model for the whole particle system is defined. Thus, an abstract class can be implemented, which, given implementations of the three interfaces, provides a method for realization of a whole particle system. This is indicated on the right-hand side of Figure 5. Note that this concept has the great advantage that all the different implementations of the interfaces can be stored and (almost) arbitrarily combined with each other to generate virtual, but realistic morphologies. We also note that the three modeling approaches that have been presented in [10], [11] and [12] can be implemented using specific, rather sophisticated implementations of the interfaces described above. Moreover, note that periodic boundary conditions are applied. This is a big advantage when applying numerical transport simulations to the model realizations, because no transport limitations at the boundary of the structures distort the results.

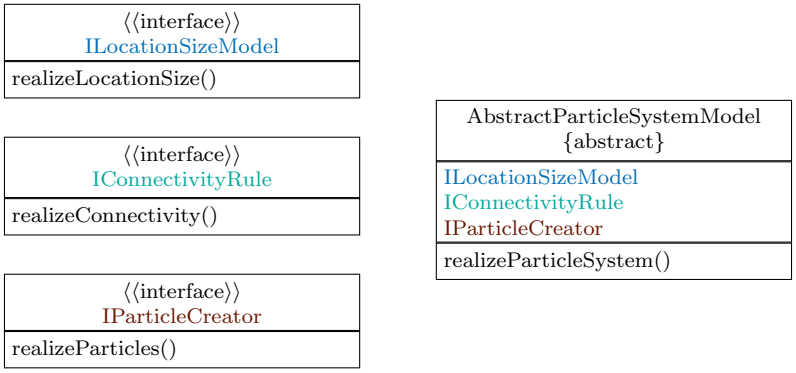

Figure 5: Simplified class diagram of the four classes that are needed to implement the model.

3. Implementations of the modeling framework for various kinds of electrodes

In this section, we give three further examples of implementations of the modeling framework. Each implementation is tailored to a specific kind of electrode. In all cases, a comparison of structural characteristics computed for model realizations and tomographic image data indicates a good fit of the model realizations to real data. Note that the three examples under consideration are the electrodes for which stochastic 3D microstructure models have been proposed in [10, 11, 12], which are simplified in the present paper. Therefore, structural characteristics of model realizations drawn from the models described in [10, 11, 12] are compared to the simplified version described in the present paper. It turns out that the model realizations resemble the properties that are found in the tomographic image data. Altogether, the goodness of fit of the simplified modeling framework described in the present paper is comparable to the models described in [10, 11, 12].

3.1. Energy cell anode

The first electrode under consideration is an anode from a lithium-ion battery. For details, see [10]. In this electrode, the volume fraction of the particle phase is rather high, namely 73.4%. In the following, an implementation of the three modules of the modeling framework proposed in the present paper is described which allows for the realization of model structures that are similar to those observed in tomographic image data for this kind of electrodes.

Locations and sizes of particles. To model the approximate locations and sizes of particles, the force-biased algorithm is used. However, such a packing of spheres only works well for a packing density up to approximately 65%, whereas we have $\xi = 0.734$ here. We solve this problem by simulating systems of slightly overlapping spheres as described in [22]. The idea is to scale the spheres by a so-called core-shell ratio γ before applying the force-biased algorithm, and then

scale the system of non-overlapping spheres back such that they are slightly overlapping, where the degree of overlap depends on the core-shell ratio γ. The core-shell ratio is computed such that the packing density for the scaled sphere system is 0.6, which results in $\gamma = 0.935$. The particle size distribution is estimated from tomographic image data and a mixed gamma distribution is fitted, which results in $k_1 = 14.19$, $\theta_1 = 0.31$, $k_2 = 4.89$, $\theta_2 = 1.87$ and a mixing parameter $\lambda = 0.38$. This means that with probability λ, the particle size is gamma distributed with shape parameter k_1 and scale parameter θ_1, and with probability $1 - \lambda$, it is gamma distributed with shape parameter k_2 and scale parameter θ_2.

Connectivity rule. The connectivity graph G is computed as the minimum spanning tree as described in Section 2.3 using $\kappa = 15$.

Modeling of particle shapes. The angular power spectrum of the particles in the electrode under consideration has already been estimated in [10], where the function given in (1) is used with $a = 0.4241, b = 0.356, c = -3.858$ and $d = 3.903$. In [10], the parameter L was chosen to be $L = 14$. Note that L determines the number of constraints that can be made in the conditional normal distribution, i.e., how many points the particle has to touch. As in the procedure described in the present paper by the minimum spanning tree G only rather few constraints are made, L can be chosen much smaller, which leads to a better accordance regarding the specific surface area of the final structure. Here, we choose $L = 6$. The points that particles have to touch in order to achieve the connectivity indicated by G are placed as described in Section 2.4, see also Figure 3, if the corresponding spheres do not intersect with each other. If they do intersect, the point which both particles have to touch is placed in the center of their intersection. Note that due to the small overlap of spheres, also particles (with a mean radius equal to the radius of the corresponding sphere) overlap more than they do for systems of non-overlapping spheres, leading to a lower volume fraction of the particle phase. This can be overcome by introducing a correction factor $\rho > 0$ as it has been done in [10]. Each sphere $(S_i, R_i) \in \Xi$ is then replaced by a particle with mean volume-equivalent radius ρR_i. The correction factor ρ has to be determined only once for a given parameter constellation. This can be easily done using the bisection method, i.e., systematically creating model realizations with varying ρ until the error regarding the volume fraction of the particle phase is smaller than a pre-defined threshold. Here, we get $\rho = 1.0156$. Moreover, as in this energy cell anode microstructure many small particles occur, the number of repetitions in the acceptance-rejection method before placing a sphere is set to $\eta = 10$ to lower computation time. The structure is finally discretized on a voxel grid of $400 \times 400 \times 119$ voxels with a voxel side length of 440nm, which corresponds to the resolution of the tomographic image data. Finally, as in [10], a closing with radius 1 is performed on the discretized structure.

Note that the modeling procedure described above differs from that one considered for the example structure in Section 2.5 (despite from actual values of

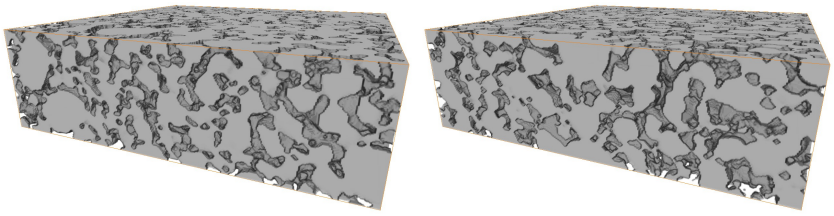

(a) (b)

Figure 6: 3D visualizations of (a) a cutout from tomographic image data and (b) a model realization for the energy cell anode.

	tomography	model realizations
volume fraction	0.734	0.733
specific surface area (1/µm)	0.295	0.292
mean sphericity	0.83	0.86
specific integral of mean curvature	-0.00855	-0.00700
specific Euler characteristic	-0.00030	-0.00031

Table 1: Comparison of characteristics of tomographic image data and corresponding model realizations for the energy cell anode.

parameters and the distribution type of the particle size distribution) only by the fact that in the first step the spheres can slightly overlap, the resulting need for a correction factor ρ and the closing step. Nevertheless, a good accordance with tomographic image data can be observed in the visual comparison given in Figure 6(a) and 6(b). In addition to the visual comparison, also structural characteristics have been compared between tomographic image data and model realizations, see Table 1. First of all, note that the volume fraction of the particle phase is approximately matched, which is also true for the specific surface area. In addition, the mean sphericity of particles is in good agreement with the one observed for particles extracted from tomographic image data. Moreover, we consider the specific integral of mean curvature and the specific Euler characteristic, see [23], which are also in good agreement. In addition to these aggregated values, we consider distributions of particle characteristics. The particle size distribution is in accordance with the results extracted from image data, see Figure 7(a). Also the distribution of the coordination number, i.e., how many particles each particle is in contact with, resembles the situation in the tomographic image data. Note that the latter characteristic has not directly been fitted (only a minimum spanning tree has been predefined for particle connectivity), but is rather a result of the sphere packing approach. Finally, we consider more detailed morphological characteristics, one characteristic of the particle phase and one characteristic of the void phase, respectively. The estimated probability density of chord lengths (see [24] for details) approximately matches between tomographic image data and model realizations, see

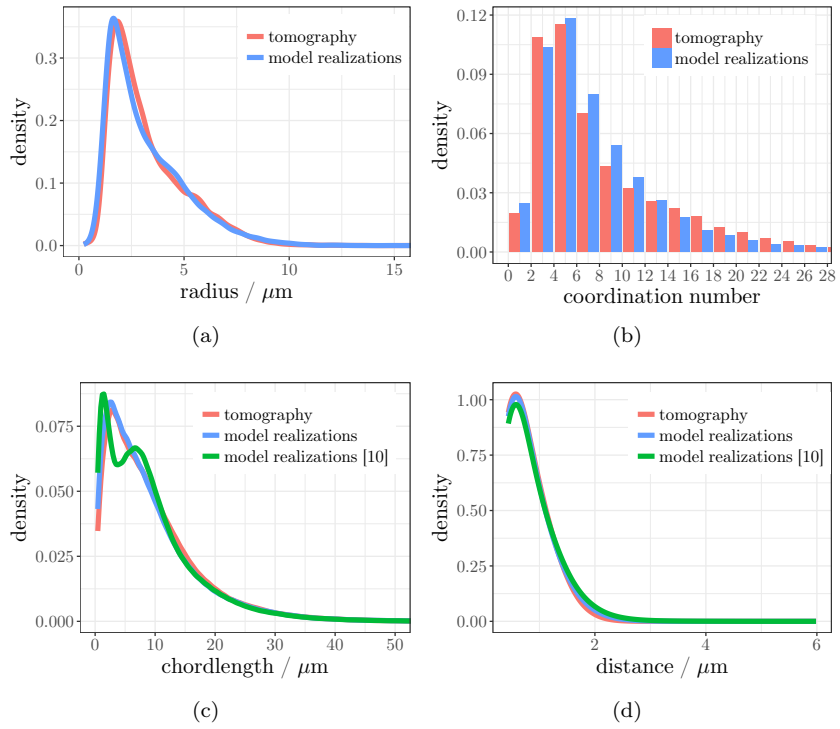

Figure 7: Comparison of image characteristics computed from tomographic image data and from model realizations for the energy cell anode. Distribution of (a) particle sizes, (b) coordination numbers, (c) chord lengths, and (d) spherical contact distances.

Figure 7(c). Note that we only consider the chord length distribution in one horizontal direction, because the model is isotropic. As can be seen in Figure 7(d), the same good match holds true for the estimated probability density of spherical contact distances, see [25]. Note that this characteristic can be considered in both phases. Here, we consider distances from the remaining phase, i.e., outside of active particles, which consists of binder, additives and pores, and will be called bap-space in the following. This information is related to the pore sizes. As can be seen from the green lines in Figure 7(c) and 7(d), for the chord lengths (especially for short chords) as well as for spherical contact distances (especially for larger distances) the fit is slightly better compared to the one of the model considered in [10].

3.2. Power cell anode

The microstructure of power cell anodes remarkably differs from those observed in energy cells, see, e.g., [26]. The main difference is the considerably lower volume fraction of the particle phase. To account for this, in [11] the model introduced in [10] has been extended to model the microstructure in power cell anodes. Moreover, the data set under consideration exhibited an anisotropic structure, with particles being rather elongated and predominantly connected in horizontal direction. In the following, an implementation of the modeling framework described in the present paper is demonstrated which allows to generate virtual microstructures the morphological properties of which resemble the tomographic image data from [11].

Locations and sizes of particles. Locations and sizes of particles are modeled using the method described in Section 2.2 without any extension, i.e., a sphere packing is performed, where the only parameters are the packing density and the sphere size distribution. The packing density is chosen according to the desired volume fraction, resulting in $\xi = 0.416$. The distribution of sphere sizes is chosen according to the particle size distribution $\mathcal{R}$ of the material, which can be modeled using a mixed gamma distribution with $k_1 = 14.19$, $\theta_1 = 0.31$, $k_2 = 4.89$, $\theta_2 = 1.87$ and mixing parameter $\lambda = 0.38$.

Connectivity rule. The anisotropy mentioned above is integrated into the model by a special construction of the connectivity graph. To begin with (for practically always ensuring complete connectivity), a minimum spanning tree is computed. As the sphere packing is not as dense as for the energy cell (due to the lower volume fraction of the spheres), it will more often be the case that particles are supposed to touch each other even if there is a certain distance between the corresponding spheres. Therefore, the points which both particles have to touch to ensure their connectivity are chosen in a slightly different way. Let (S_1, R_1) and (S_2, R_2) be two spheres the corresponding particles of which are supposed to touch each other. Then the point $\zeta_{1,2}$ which both particles have to touch is chosen as the (uniquely determined) point in space with minimum distance to S_1 and S_2 such that $||S_1 - \zeta_{1,2}||/R_1 = ||S_2 - \zeta_{1,2}||/R_2$. By this choice of $\zeta_{1,2}$ it is achieved that larger particles have to expand more towards the point

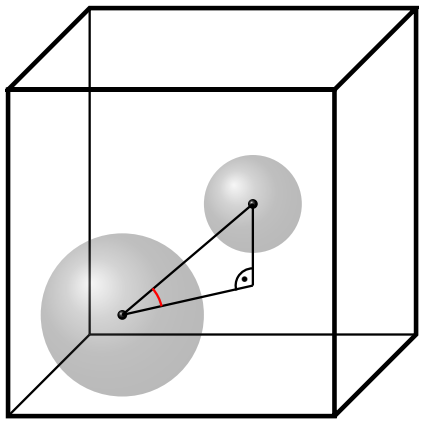

Figure 8: Sketch showing the angle between two sphere centers, which is considered for including anisotropy.

that has to be touched than smaller particles. This motivates to weight the edges between two spheres (S_i, R_i) and (S_i, R_j) of the graph G' from which the minimum spanning tree is computed by $||S_i - \zeta_{i,j}/||R_i$ (which is equal to $||S_j - \zeta_{i,j}||/R_j$ due to the definition of $\zeta_{i,j}$). Based on these edge weights, a minimum spanning tree is computed as described in Section 2.3. This minimum spanning tree is denoted by G^*. Note that G^* does not yet include anisotropy into the model. Therefore, we now weight the edges of G^* by the angle between a horizontal plane and the segment between the two corresponding sphere centers, see the angle marked using red color in Figure 8. Note that the same edge weighting has been used in [11] to include anisotropy, however, the construction of the connectivity graph was more complex. Moreover, we add a weighted (depending on the angle) edge to G^* if the edge weight in G' is less than a threshold δ, where we found that $\delta = 0.2$ leads to reasonable results. Note that δ has a geometrical interpretation, i.e., if $\delta = 0.2$, particles have to expand by 20% of their mean radius towards the point which they have to touch to fulfill the connectivity conditions. Finally, based on G^*, a minimum spanning tree G is computed. The procedure described above ensures that (a) particles are rather elongated and predominantly connected in horizontal direction, as the minimum spanning tree was computed based on edge weights depending on the angle, (b) no particles that are too far away from each other have to touch each other, i.e., most particles have to expand by not more than 20% of their mean volume-equivalent radius and (c) the whole system of particles is completely connected.

Modeling of particle shapes. Particles are finally modeled as described in Section 2.4 with parameters as in [11], namely $L = 10, a = 0.615, b = 0.047, c = -3.642$ and $d = 3.398$. The only difference to Section 2.4 is the choice of points $\zeta_{i,j}$ which particles have to touch as decribed in the previous paragraph. As in [11], the structure is discretized on a voxel grid of $400 \times 400 \times 109$ voxels with a voxel

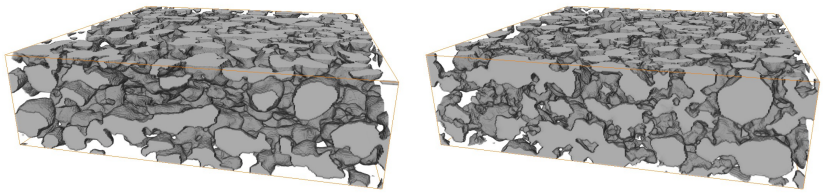

(a) (b)

Figure 9: 3D visualizations of (a) a cutout from tomographic image data and (b) a model realization for the power cell anode.

	tomography	model realizations
volume fraction	0.416	0.424
specific surface area (1/µm)	0.197	0.199
mean sphericity	0.84	0.85
specific integral of mean curvature	0.00303	0.00315
specific Euler characteristic	-0.00004	-0.00005

Table 2: Comparison of characteristics of tomographic image data and corresponding model realizations for the power cell anode.

side length of 440nm, and a closing with radius 2 is performed.

Again, we compare model realizations to tomographic image data to investigate the goodness of fit of the model. A comparison of 3D visualizations (see Figure 9(a) and 9(b)) indicates that the elongation of particles in horizontal direction is resembled. From Table 2, we see that the volume fraction of the simulated particle phase is slightly larger than the desired value. This difference results from the fact that when sampling the particles from a conditional distribution (given points in space which they have to touch), their volume can become a little larger than desired on average. In [11], this problem was overcome by using a correction factor as described in Section 3.1. However, as the difference is rather small and, moreover, the particle size distribution (see Figure 10(a)) is nevertheless approximately matched, no correction factor is used in the present paper. Moreover, the mean specific surface area of the model realizations almost perfectly matches the specific surface area of the tomographic image data. Also the mean sphericity of particles is in good agreement with the one observed for particles extracted from tomographic image data. Also the specific integral of mean curvature and the specific Euler characteristic are in good agreement. In addition, the distributions of coordination numbers match almost perfectly, see Figure 10(b). Again, note that (as for the energy cell anode) this property has not been directly adjusted, but is a result of the sphere packing procedure.

Furthermore, we compare the estimated probability density of chord lengths and the probability density of spherical contact distances of model realizations

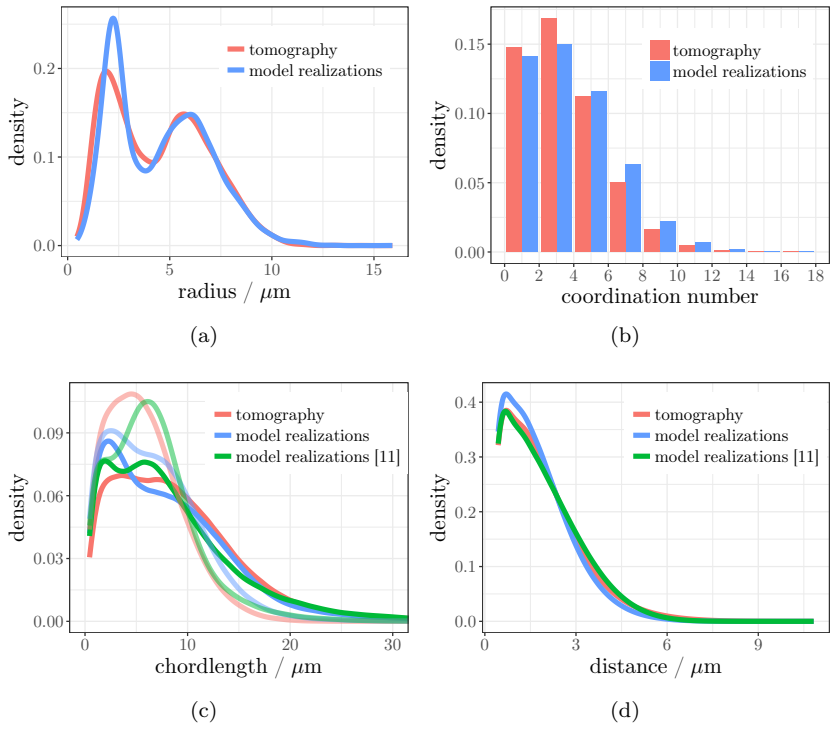

Figure 10: Comparison of image characteristics computed from tomographic image data and from model realizations for the power cell anode. Distribution of (a) particle sizes, (b) coordination numbers, (c) chord lengths, and (d) spherical contact distances.

and tomographic image data. In addition, the results for structures drawn from the model considered in [11] are shown. The density of chord lengths (see Figure 10(c)) is considered in horizontal (continuous line) and vertical (shaded line) direction. The difference between the two directions is an indicator for the anisotropy of the structure, which we find to be resembled by the model. Only in vertical direction, the fit is slightly worse than in [11], however still being in a reasonable range, especially when considering the considerable simplification of the model described in the present paper compared to the model considered in [11]. Moreover, the density of spherical contact distances from the bap-phase of the tomographic image data (see Figure 10(d)) is approximately resembled by the simulated structures.

To summarize, it has been shown that the framework described in the present paper can be used to realistically describe the microstructure of power cell anodes. Comparing the implementation to the simple example structure considered in Section 2.5, only the construction of the connectivity rule has been changed to account for the anisotropy, and the points that particles have to touch to ensure that they are in contact with each other according to the conncectivity graph have been defined in a slightly different way.

3.3. Energy cell cathode

In this section we show that the modeling framework can also be used to describe the microstructure of cathodes. In [12], the ideas developed in [10, 11] have been further extended to model cathode microstructures, which have rather spherical particles and a low volume fraction of active material. However, the model considered in [12] is rather complicated with even a lot more parameters than in [10] and [11]. We show that a much simpler model using the framework described in the present paper can be used, which leads to a comparable fit with respect to several microstructural characteristics. The extension compared to the procedure described in Section 2.5 is to explicitely model the structure of the remaining space, outside of active particles, which consists of binder, additives and pores, and is therefore called the bap-space. This can be done in the first step of the framework and is described in the following.

Locations and sizes of particles. The particle size distribution $\mathcal{R}$ can be modeled using a mixed gamma distribution with $k_1 = 14.19$, $\theta_1 = 0.31$, $k_2 = 4.89$, $\theta_2 = 1.87$ and mixing parameter $\lambda = 0.38$. The packing density $\xi = 0.336$ is chosen according to the volume fraction of the active particle system. The rather low volume fraction of the particle system induces a specific structure of the bap-phase. This structure is taken into account by additionally including spheres in the first step which are not replaced by particles, but form the bap-phase of the electrode. To define their size distribution, we describe the bap-phase of the tomographic image data by non-overlapping spheres as follows. We start with the largest sphere that can be put into the bap-phase without intersecting with any particle. Given this sphere, we look for the second largest sphere that does neither intersect with the first sphere nor with any particle. This procedure is repeated until the volume fraction of particles together with the bap-spheres

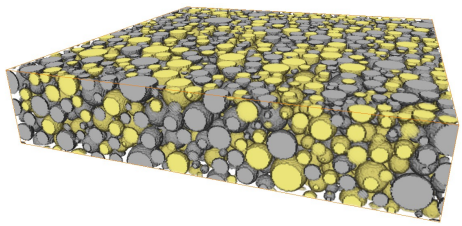

Figure 11: Example of a system of non-overlapping spheres for the generation of a cathode microstructure. Grey: Spheres that will be replaced by a particle. Yellow: Spheres representing bap-volume.

exceeds a threshold of 60%. Then we estimate the distribution function of the sphere radii. It turns out that they can be described by a gamma distribution with parameters $k = 1.26$ and $\theta = 1.9$, which is shifted by 5.83 and truncated at 17.47. Then, after sampling spheres from $\mathcal{R}$ for the initial configuration on which the force-biased algorithm is performed, we sample spheres from the distribution of spheres describing the bap-phase and add them to the initial configuration until a volume fraction of 60% is reached. Then the force-biased algorithm is performed to achieve a structure with non-overlapping spheres. An example can be found in Figure 11, where grey spheres show those drawn from $\mathcal{R}$ and yellow spheres show those representing the bap-spheres. Later on, only the grey spheres will be replaced by particles, while the yellow spheres ensure that the pore size distribution of the bap-phase of the real data set is resembled by the model.

Connectivity rule. When considering the tomographic image data, it turns out that the particle system is not completely connected. This is due to the fact that more additives (which are not visible in the images) are added to cathodes because of the bad conductivity of the active material. Therefore, we do not construct a connectivity graph in the cathode model, i.e., each particle is sampled independently of its neighbourhood. It turns out that nevertheless a reasonable particle connectivity is achieved, because particles induced by neighbouring spheres will be in contact with a certain probability even this is not predefined by a connectivity graph.

Modeling of particle shapes. Particles are finally modeled as described in Section 2.4 with parameters of the angular power spectrum as in [12], namely $a = 1027, b = 0.2411, c = -4.009$ and $d = 4.206$. The series expansion parameter L is chosen to be $L = 4$. This small value leads to rather regular particles as they are observed in the tomographic image data. As in [12], the structure is discretized on a voxel grid of $400 \times 400 \times 80$ voxels with a voxel side length of 440nm.

To summarize, the specific features of the cathode model in constrast to the basic model described in Section 2 are that additional spheres are added in the first step to model the structure of the bap-phase, and that no particle

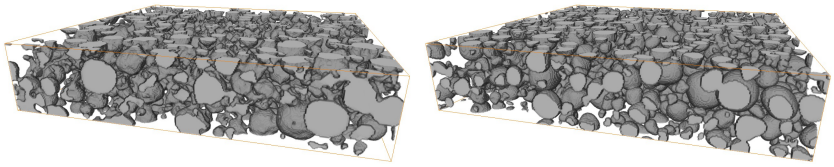

(a) (b)

Figure 12: 3D visualizations of (a) a cutout from tomographic image data and (b) a model realization for the energy cell cathode.

	tomography	model realizations
volume fraction	0.336	0.334
specific surface area (1/µm)	0.198	0.229
mean sphericity	0.90	0.92
specific integral of mean curvature	0.00622	0.00832
specific Euler characteristic	-0.00003	-0.00018

Table 3: Comparison of characteristics of tomographic image data and corresponding model realizations for the energy cell cathode.

connectivity is predefined by a connectivity graph. In Figure 12(a) and 12(b), a visual comparison between tomographic image data and a model realization is given. In Table 3, it can be seen that the volume fraction of the particle phase is approximately matched. The mean specific surface area of active material in the model realizations is a bit larger than the one estimated from tomographic image data. An additional closing (as it has also been done in [12] of the discretized image would lower the surface area. However, this step is skipped in the present paper, because it can change the volume fraction of the particle phase, which would make it necessary to include a correction factor ρ as in Section 3.1. In addition, the mean sphericity of particles is in good agreement with the one observed for particles extracted from tomographic image data. While there is a slight difference of the specific integral of mean curvature, a larger deviation of the specific Euler characteristic can be observed. However, the structural characteristics shown in Figure 13 indicate that many structural characteristics (which are important for the functionality of a battery) are matched. The particle size distribution (see Figure 13(a)) is approximately matched, and the distribution of the coordination number regarding particle connectivity (see Figure 13(b)) is also close to the one observed in tomographic image data, although no connectivity has been predefined. Furthermore, we again consider the estimated probability density of chord lengths as well as the spherical contact distances in the bap-phase. While the latter one matches well with its counterpart estimated from tomographic image data (see Figure 13(d), there is a slight deviation for the chord lengths (see Figure 13(c)). This characteristic was matched a bit better by the model described in [12], however, we again emphasize the considerably lower amount of parameters of the model described

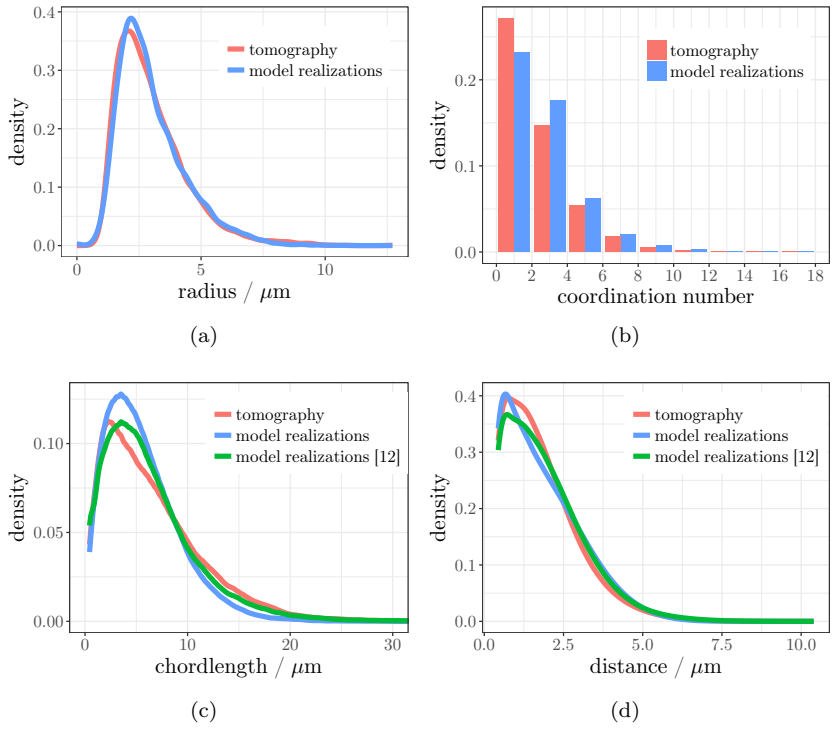

Figure 13: Comparison of image characteristics computed from tomographic image data and from model realizations for the energy cell cathode. Distribution of (a) particle sizes, (b) coordination numbers, (c) chord lengths, and (d) spherical contact distances.

in the present paper, as well as the geometrical interpretation, which makes the model suitable for virtual materials testing. If a better fit of the chord length distribution function is desired, the model can be extended. In particular, the closing step that has not been performed would eliminate small chords, leading to a distribution that is closer to the one obtained for tomographic image data.

4. Applications to virtual materials design

In Section 3 the flexibility of the modeling framework as well as its ability to reproduce the structural features of given tomographic image data has been shown. We now demonstrate how the fact that the modeling framework is less complicated than the approaches proposed in [10, 11, 12] can be used to systematically design virtual electrode microstructures on the computer. First, it is shown how the particle size distribution can be changed for structures as discussed in Section 3.2, keeping other characteristics fixed, see Section 4.1. Then, the design of a two-layer electrode with different structural properties in the top layer compared to the bottom layer is shown, see Section 4.2. Further examples are given in the supplementary information.

4.1. Varying the particle size distribution

A first simple task that can be performed using the framework described in the present paper is to change the particle size distribution, while keeping the volume fraction of active material fixed. This means that we have to define a different distribution $\mathcal{R}$. We use the same implementation and parameters as in Section 3.2, but change the particle size distribution $\mathcal{R}$ to a gamma distribution with parameters $k = 15$ and $\theta = 1$. The resulting structure is shown in Figure 14(a). The volume fraction of the active particle phase of the structure is 42.1%, which approximately matches the predefined one. In Figure 14(b) it can be seen that the predefined particle size distribution (black line), which strongly differs from the one estimated from tomographic image data (red line) is approximately matched in the simulated structure (blue line). Moreover, the mean sphericity of particles (0.84) is still in agreement with the one estimated from tomographic image data.

4.2. Two-layer electrodes

Another possibility to improve transport properties of lithium-ion batteries is to use layered electrodes, see, e.g., [27]. After casting and drying of the first layer, a second layer is added. This allows us to vary structural properties between first and second layer. Therefore, we use the modeling framework described in the present paper to simulate an electrode microstructure with different particle size distribution and volume fraction of the particle phase in the top and bottom part, respectively.

In the first step, we use the force-biased algorithm to generate a system of non-overlapping spheres in the bottom part of the sampling window. We use a truncated and shifted gamma distribution for the sphere size distribution,

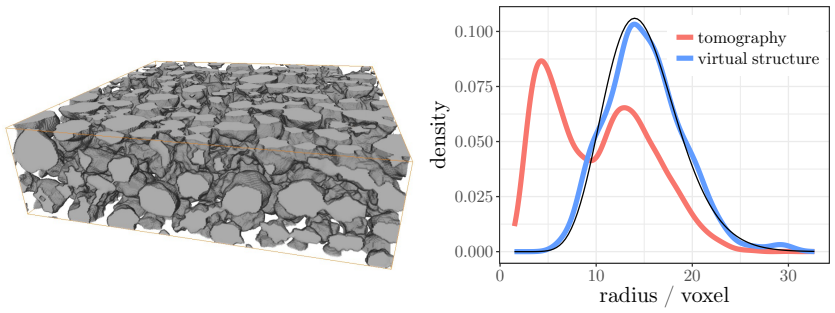

(a) (b)

Figure 14: (a) 3D visualization of a model realization of the power cell model with different particle size distribution. (b) Particle size distribution estimated from tomographic image data (red) compared to the virtual structure (blue). The black line shows the predefined distribution.

i.e., a gamma distribution with shape parameter $k_b = 4$ and scale parameter $\theta_b = 2$, that is shifted by $s_b = 10$ and truncated at $t_b = 30$. The packing density was chosen as $\xi_1 = 0.6$. For the sphere size distribution of the top layer, we choose a truncated and shifted gamma distribution with shape parameter $k_t = 2$ and scale parameter $\theta_t = 2$, that is shifted by $s_t = 3$ and truncated at $t_t = 20$. However, for the top layer, the force biased algorithm is only applied in a subwindow of the upper part of the sampling window, such that no intersection of spheres between the lower and upper part is possible. The region which is not considered is subsequently filled with spheres following the same size distribution as the other spheres in the top layer. However, no collective rearrangement algorithm is applied, but spheres are placed using an acceptance-rejection method. This means that for each sphere, first a radius is drawn, and then a location is simulated uniformly such that no intersection with the remaining spheres is caused. This is done by sampling up to 10 000 times, until a location which does not cause any overlap is found. In the unlikely case that after 10 000 iterations no location is found, a new radius is drawn from the distribution described above. Note that this might lead to a preference of smaller spheres. However, in our simulations, no radius was rejected, i.e., after at least 10 000 tries a suitable location was found. Even if, for other parameter constellations, rejection of a radius does occur, it can be interpreted to mimic the fact that smaller particles fill the gaps that are generated by the larger particles of the bottom layer. Spheres are added until the packing density ξ_2 of the top layer is reached, which is chosen to be $\xi_2 = 0.4$. Note that the random allocation of spheres can also be generated by consistently using a collective rearrangement algorithm like the force-biased algorithm. However, the explicit placing of spheres allows to control the behaviour of particles at the interface between the two layers. This is of advantage if effects at this interface are of interest, as they have e.g. been investigated in [28].

Given the random allocation of spheres, the connectivity graph G is constructed as the minimum spanning tree described in Section 2.3. Particles are finally simulated using the same angular power spectrum as in Section 3.3 with $L = 10$.

A visualization of the outcome of the algorithm described above is visualized in Figure 15(a). Note that the predefined particle size distribution functions in

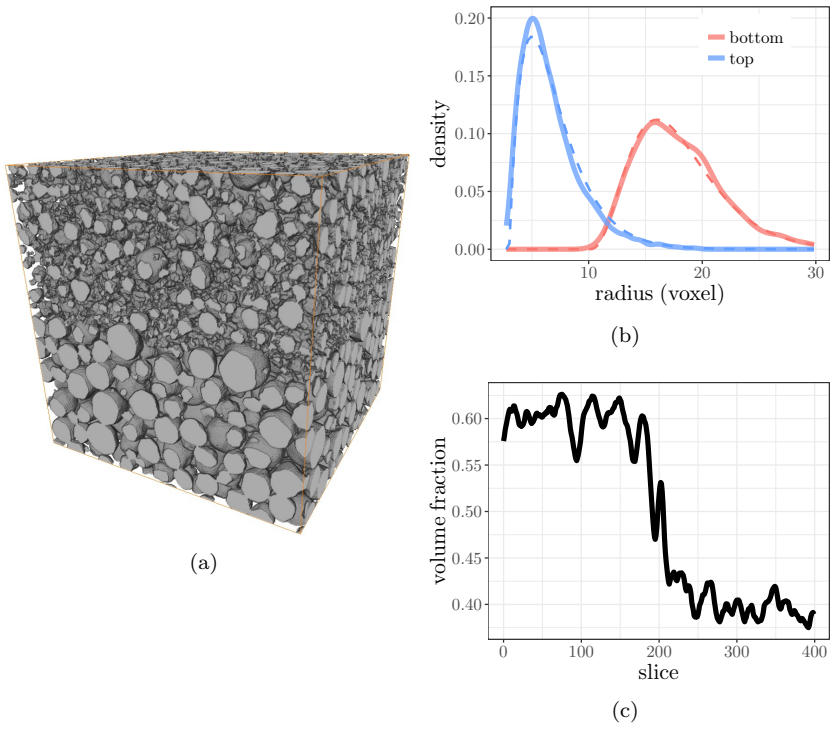

Figure 15: (a) 3D visualization of a model realization of a two-layer electrode. (b) Particle size distributions (continuous lines) together with predefined distributions (dashed lines). (c) Volume fractions of the active particle phase per slice of the 3D image stack (from bottom to top).

the top and bottom part are matched, see Figure 15(b), and also the local volume fractions approximately correspond to the values of ξ_1 and ξ_2, see Figure 15(c). Therefore, we conclude that the framework described in the present paper allows us to generate multi-layer electrodes with predefined local volume fractions and particle size distributions, which can subsequently be investigated regarding their electrochemical performance, using e.g. spatially resolved numerical transport simulations [29].

5. Conclusions and outlook

In the present paper, a framework for stochastic 3D modeling of the microstructure of battery electrodes has been presented. The framework is based on models proposed in recent publications ([10, 11, 12]), but significiantly simplifies these models, while providing a similar good fit of structural characteristics when fitted to tomographic image data for various kinds of electrodes. In particular, the (fewer) model parameters mainly have (in contrast to the models described in [10, 11, 12]) a direct geometrical interpretation, which, e.g., allows to explicitely control the particle size distribution. Moreover, the framework is constructed in a modular way, where the three modules control different aspects of the resulting microstructure. The fact that the number of model parameters is reduced, while they have a direct geometrical interpretation, combined with the modular concept allows to more systematically perform virtual materials design, i.e., to make use of the models to generate virtual, but realistic electrode microstructures. To give an example, it has been shown how to generate two-layer electrodes, where the volume fraction of active material as well as the particle size distribution differ in the bottom and top part of the electrode, respectively. Such virtual microstructures can then be used as input for spatially resolved transport simulations, which allows us to identify promising design concepts that can improve the functionality of batteries.

Due to the modular concept, it is easily possible to improve individual steps of the modeling framework. To give some ideas for further extensions, which could be subject of further research, the estimation of the angular power spectrum could be conditioned on the particle size, such that (possibly differing) shapes of smaller and larger particles can be modeled individually. This can also be used to prevent that small particles have to be replaced by spheres, which can eliminate the difference in the distribution of sphericity between real and simulated data. Moreover, it is possible to enlarge the contact areas between particles by forcing them not only to touch one common point, but several ones.

Possible ideas for future work include the electrochemical validation, as it has e.g. been done in [29]. Moreover, the modeling framework can finally be used to generate a broad range of virtual, but realistic microstructures, which allows us to investigate relationships between microstructure and performance of lithium-ion battery electrodes. A first outlook to possible virtual structures (despite from the ones presented in Section 4) is given in the supplementary material.

Acknowledgements

This work was partially funded by BMBF under grant number 03XP0073E.

References

[1] G.-A. Nazri, G. Pistoia (Eds.), Lithium Batteries: Science and Technology, Springer, New York, 2003.

[2] M. M. Thackeray, C. Wolverton, E. D. Isaacs, Electrical energy storage for transportation – approaching the limits of, and going beyond, lithium-ion batteries, Energy & Environmental Science 5 (7) (2012) 7854–7863. doi:10.1039/C2EE21892E.

[3] J. R. Wilson, J. S. Cronin, S. A. Barnett, S. J. Harris, Measurement of three-dimensional microstructure in a $LiCoO_2$ positive electrode, Journal of Power Sources 196 (7) (2011) 3443–3447. doi:10.1016/j.jpowsour.2010.04.066.

[4] R. E. García, Y.-M. Chiang, W. Craig Carter, P. Limthongkul, C. M. Bishop, Microstructural modeling and design of rechargeable lithium-ion batteries, Journal of The Electrochemical Society 152 (1) (2005) A255–A263. doi:10.1149/1.1836132.

[5] A. Latz, J. Zausch, Thermodynamic consistent transport theory of Li-ion batteries, Journal of Power Sources 196 (6) (2011) 3296–3302. doi:10.1016/j.jpowsour.2010.11.088.

[6] T. Danner, M. Singh, S. Hein, J. Kaiser, H. Hahn, A. Latz, Thick electrodes for Li-ion batteries: A model based analysis, Journal of Power Sources 334 (2016) 191–201. doi:10.1016/j.jpowsour.2016.09.143.

[7] D. Marinucci, G. Peccati, Random Fields on the Sphere: Representation, Limit Theorems and Cosmological Applications, Cambridge University Press, Cambridge, 2011.

[8] X. Liu, E. Garboczi, M. Grigoriu, Y. Lu, S. T. Erdoğan, Spherical harmonic-based random fields based on real particle 3D data: Improved numerical algorithm and quantitative comparison to real particles, Powder Technology 207 (1) (2011) 78–86. doi:10.1016/j.powtec.2010.10.012.

[9] J. Feinauer, A. Spettl, I. Manke, S. Strege, A. Kwade, A. Pott, V. Schmidt, Structural characterization of particle systems using spherical harmonics, Materials Characterization 106 (2015) 123–133. doi:10.1016/j.matchar.2015.05.023.

[10] J. Feinauer, T. Brereton, A. Spettl, M. Weber, I. Manke, V. Schmidt, Stochastic 3D modeling of the microstructure of lithium-ion battery anodes via Gaussian random fields on the sphere, Computational Materials Science 109 (2015) 137–146. doi:10.1016/j.commatsci.2015.06.025.

[11] D. Westhoff, J. Feinauer, K. Kuchler, T. Mitsch, I. Manke, A. Latz, V. Schmidt, Parametric stochastic 3D model for the microstructure of anodes in lithium-ion power cells, Computational Materials Science 126 (2017) 435–467. doi:10.1016/j.commatsci.2016.09.006.

[12] K. Kuchler, D. Westhoff, J. Feinauer, T. Mitsch, I. Manke, V. Schmidt, Stochastic model for the 3D microstructure of pristine and cyclically aged

cathodes in Li-ion batteries, Modelling and Simulation in Materials Science and Enginnering 26 (2018) 035005. doi:10.1088/1361-651X/aaa6da.

[13] S. N. Chiu, D. Stoyan, W. S. Kendall, J. Mecke, Stochastic Geometry and its Applications, 3rd Edition, J. Wiley & Sons, Chichester, 2013.

[14] C. Lautensack, Random Laguerre Tessellations, Ph.D. thesis, Karlsruhe Institute of Technology (2007).

[15] R. Diestel, Graph Theory, Springer, Berlin, 2010.

[16] J. Mościński, M. Bargieł, Z. A. Rycerz, P. W. M. Jacobs, The force-biased algorithm for the irregular close packing of equal hard spheres, Molecular Simulation 3 (1989) 201–212. doi:10.1080/08927028908031373.

[17] A. Bezrukov, M. Bargieł, D. Stoyan, Statistical analysis of simulated random packings of spheres, Particle & Particle Systems Characterization 19 (2) (2002) 111–118. doi:10.1002/1521-4117(200205)19:2<111::AID-PPSC111>3.0.CO;2-M.

[18] J. Illian, A. Penttinen, H. Stoyan, D. Stoyan, Statistical Analysis and Modelling of Spatial Point Patterns, J. Wiley & Sons, Chichester, 2008.

[19] R. C. Prim, Shortest connection networks and some generalizations, Bell System Technical Journal 36 (6) (1957) 1389–1401. doi:10.1002/j.1538-7305.1957.tb01515.x.

[20] A. Lang, C. Schwab, Isotropic Gaussian random fields on the sphere: Regularity, fast simulation and stochastic partial differential equations, The Annals of Applied Probability 25 (6) (2015) 3047–3094. doi:10.1214/14-AAP1067.

[21] J. Mayer, V. Schmidt, F. Schweiggert, A unified simulation framework for spatial stochastic models, Simulation Modelling Practice and Theory 12 (2004) 307–326. doi:10.1016/j.simpat.2004.02.001.

[22] A. Spettl, R. Wimmer, T. Werz, H. Heinze, S. Odenbach, C. E. Krill, V. Schmidt, Stochastic 3D modeling of Ostwald ripening at ultra-high volume fractions of the coarsening phase, Modelling and Simulation in Materials Science and Engineering 23 (2015) 065001. doi:10.1088/0965-0393/23/6/065001.

[23] J. Ohser, K. Schladitz, 3D Images of Materials Structures: Processing and Analysis, Wiley-VCH, Weinheim, 2009.

[24] J. Ohser, F. Mücklich, Statistical Analysis of Microstructures in Materials Science, J. Wiley & Sons, Chichester, 2000.

[25] D. Stoyan, A. Wagner, H. Hermann, A. Elsner, Statistical characterization of the pore space of random systems of hard spheres, Journal of Non-Crystalline Solids 357 (6) (2011) 1508–1515. doi:10.1016/j.jnoncrysol.2010.12.033.

[26] M. Ender, J. Joos, A. Weber, E. Ivers-Tiffe, Anode microstructures from high-energy and high-power lithium-ion cylindrical cells obtained by X-ray nano-tomography, Journal of Power Sources 269 (2014) 912–919. doi:10.1016/j.jpowsour.2014.07.070.

[27] J. Whitacre, K. Zaghib, W. West, B. Ratnakumar, Dual active material composite cathode structures for Li-ion batteries, Journal of Power Sources 177 (2) (2008) 528–536. doi:10.1016/j.jpowsour.2007.11.076.

[28] D. Westhoff, T. Danner, S. Hein, A. Hoffmann, R. Scurtu, L. Kremer, A. Hilger, I. Manke, M. Wohlfahrt-Mehrens, A. Latz, V. Schmidt, Analysis of microstructural effects in multi-layer lithium-ion battery cathodes, Materials Characterization (submitted).

[29] S. Hein, J. Feinauer, D. Westhoff, I. Manke, V. Schmidt, A. Latz, Stochastic microstructure modeling and electrochemical simulation of lithium-ion cell anodes in 3D, Journal of Power Sources 336 (2016) 161–171. doi:10.1016/j.jpowsour.2016.10.057.